

Holotoxin Disassembly by Protein Disulfide Isomerase Is Less Efficient for Escherichia Coli Heat-labile Enterotoxin Than Cholera Toxin

Albert Serrano

University of Central Florida

Jessica L. Guyette

University of Central Florida

Joel B. Heim

University of Oslo

Michael Taylor

University of Central Florida

Patrick Cherubin

University of Central Florida

Ute Krengel

University of Oslo

Ken Teter

University of Central Florida

Suren Tatulian (✉ statulia@ucf.edu)

University of Central Florida

Research Article

Keywords: Cholera toxin (CT), protein disulfide isomerase (PDI), cell surface, PDI-toxin interactions

Posted Date: September 23rd, 2021

DOI: <https://doi.org/10.21203/rs.3.rs-918594/v1>

License: © ⓘ This work is licensed under a Creative Commons Attribution 4.0 International License.

[Read Full License](#)

Version of Record: A version of this preprint was published at Scientific Reports on January 7th, 2022.
See the published version at <https://doi.org/10.1038/s41598-021-03939-9>.

1 Holotoxin disassembly by protein disulfide isomerase is less efficient for
2 *Escherichia coli* heat-labile enterotoxin than cholera toxin

3

4 Albert Serrano^{1,*}, Jessica L. Guyette^{1,*||}, Joel B. Heim², Michael Taylor¹, Patrick Cherubin^{1,¶},
5 Ute Krenzel², Ken Teter^{1,#}, and Suren A. Tatulian^{3,#}

6

7 ¹Burnett School of Biomedical Sciences, College of Medicine, University of Central Florida,
8 Orlando, FL 32816

9 ²Department of Chemistry, University of Oslo, Blindern, Norway.

10 ³Department of Physics, College of Sciences, University of Central Florida, Orlando, FL 32816

11 *These authors contributed equally to the work

12 #email: statulia@ucf.edu or Kenneth.Teter@ucf.edu

13

14

15 ||Present address: Viral Pathogenesis Section, Laboratory of Viral Diseases, National Institutes
16 of Health, Bethesda, MD

17 ¶Present address: Department of Microbiology, Perelman School of Medicine, University of
18 Pennsylvania, Philadelphia, PA

19

20

21

22

23

24

25

26

27

28

29

30

31

32

33

34

35

36

37

38

39

40

41

42

43

44

45 **ABSTRACT**

46 Cholera toxin (CT) and *Escherichia coli* heat-labile enterotoxin (LT) are structurally similar
47 AB₅-type protein toxins. They move from the cell surface to the endoplasmic reticulum where
48 the A1 catalytic subunit is separated from its holotoxin by protein disulfide isomerase (PDI), thus
49 allowing the dissociated A1 subunit to enter the cytosol for a toxic effect. Despite similar
50 mechanisms of toxicity, CT is more potent than LT. The difference has been attributed to a more
51 stable domain assembly for CT as compared to LT, but this explanation has not been directly
52 tested and is arguable as toxin disassembly is an indispensable step in the cellular action of these
53 toxins. We show here that PDI disassembles CT more efficiently than LT, which provides a
54 possible explanation for the greater potency of the former toxin. Furthermore, direct examination
55 of CT and LT domain assemblies found no difference in toxin stability. Using novel analytic
56 geometry approaches, we provide a detailed characterization of the positioning of the A subunit
57 with respect to the B₅ pentamer and demonstrate significant differences in the interdomain
58 architecture of CT and LT. Protein docking analysis further shows that these global structural
59 differences result in distinct modes of PDI-toxin interactions. Our results highlight previously
60 overlooked structural differences between CT and LT that provide a new molecular explanation
61 for the PDI-assisted disassembly and differential potency of these toxins.

62

63 **INTRODUCTION**

64 Cholera toxin (CT) and *Escherichia coli* heat-labile enterotoxin (LT) are AB₅-type protein toxins
65 that share ~82% amino acid sequence identity and a common toxicity mechanism^{1,2}. They are
66 composed of a receptor-binding pentamer of B subunits (B₅) and an A subunit. The A subunit is
67 produced as one chain and comprises an enzymatic A1 portion (amino acid residues 1-192 for
68 CT or 1-194 for LT) and an A2 portion (residues 193-240 for CT or 195-240 for LT) that enters
69 the central pore of the B₅ pentamer by its C-terminal tail and thereby provides a noncovalent
70 linkage between the A and B₅ portions. The A chain is proteolytically nicked into A1 and A2
71 parts, which stay connected through a disulfide bond between Cys187 and Cys199. Reduction of
72 the A1-A2 disulfide bond in the host cell is required for toxin activation and release of the A1
73 chain into the cytosol, where it catalyzes the ADP-ribosylation of Gs α . This results in cAMP-
74 mediated electrolyte and fluid leakage in the intestine, severe dehydration, and diarrhea³.

75 The atomic-resolution structures of various forms of CT and LT, such as wild type or mutant
76 proteins, with or without bound ligands, different crystal forms, have been determined by X-ray
77 crystallography⁴⁻¹¹. Both toxins adopt overall very similar structures, with a B₅ pentameric ring
78 and an A subunit tethered on top like a wedge. The A2 chain runs as a continuous α -helix down
79 to the orifice of the B₅ central opening and threads through the pore. Despite these common
80 conformational features, significant structural differences have been reported for the C-terminal
81 tails of the A2 subunits of LT and CT. In the LT structure, the A2 tail spans the B₅ pore as an
82 extended chain, with a 1.5-turn helix at the C-terminus⁴⁻⁹ (Protein Data Bank (PDB) IDs 1lt4,
83 1lta, 1ltg, 1lti, 1lts, and 1lth). In contrast, the C-terminal segment of A2 in the first structure of
84 CT (PDB ID 1xtc) assumes α -helix-like structure that makes extensive, mostly nonpolar contacts
85 with the pore, thus stabilizing the whole structure¹¹. However, this structure has poor geometry
86 and is not well refined. Later X-ray crystallography studies of CT show a divergent conformation
87 for the pore-spanning A2 tail which involves an elongated, non-helical structure with a 1-turn
88 helix at the end¹⁰ (PDB IDs 1s5b, 1s5c, 1s5d, 1s5e, and 1s5f). The last four or five amino acids
89 of the A2 subunit are missing in these structures because of poor electron density.

90 The functional implications of these structural details have been explored in several studies.
91 Cell culture experiments on polarized T84 intestinal epithelial cells showed that CT causes Cl⁻
92 ion secretion with nearly 2-fold faster kinetics as compared to LT^{12,13}. Extensive studies of
93 mutant and chimeric proteins concluded that the region responsible for the difference in toxicity
94 resides in an 11 amino acid sequence (226-236) near the C-terminus of the A2 subunit, where 4
95 residues differ between CT and LT¹³. It was proposed that the A2 tail provides CT with a greater
96 stability than LT, which consequently allows more CTA1 to be delivered into the host cytosol.
97 The relative stabilities of CT and LT were not directly tested, however: the supporting evidence
98 for this hypothesis was derived from studies on CT/LT hybrid toxins rather than the two native
99 toxins¹³. Still, a molecular dynamics analysis suggested more efficient nonpolar contacts
100 between the A2 tail and the central pore of the B₅ pentamer and restricted solvent intercalation
101 into the pore for CT as compared to LT, possibly contributing to the predicted higher cellular
102 stability of CT¹⁴. This conjecture is disputable, given the fact that holotoxin disassembly is a
103 critical step for toxicity.

104 Holotoxin disassembly occurs after CT and LT travel from the cell surface to the
105 endoplasmic reticulum (ER) of a target cell. Reduction of the A1/A2 disulfide bond occurs at the
106 resident redox state of the ER¹⁵, but reduction alone does not release the A1 subunit from the rest
107 of the toxin¹⁶: disassembly specifically requires the action of protein disulfide isomerase (PDI)¹⁷,
108 ¹⁸. This is hypothesized to occur by a physical mechanism in which the A1 subunit is pushed

109 away from the A2/B₅ complex by the expanded structure of PDI that results from its contact with
110 the A1 subunit¹⁹. The dissociated A1 subunit can then enter the cytosol where it modifies its Gsa
111 target.

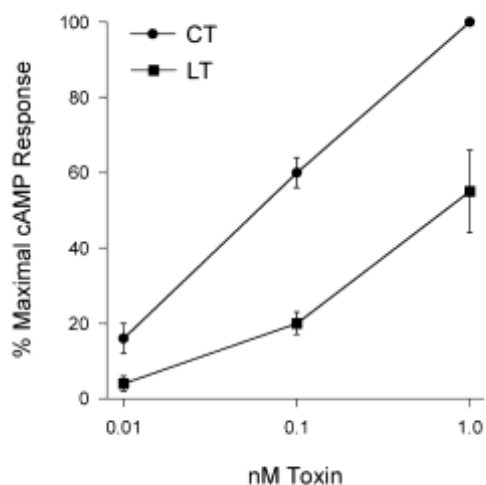
112 In this work, we adopt a new approach to the differential toxicity of CT and LT and its
113 relation to the structural features of the toxins. We show that PDI disassembles CT more
114 efficiently than LT, and this correlates with the greater cellular potency of CT in comparison to
115 LT. CT and LT did not exhibit differences in stability when subjected to an ELISA that had
116 previously detected differences in the stabilities of two CT/LT hybrid toxins used as proxies for
117 native CT and native LT. Quantitative description of the A subunit orientation for six CT and six
118 LT structures, using novel analytic geometry simulations, unveils a significant difference
119 between the tilt angles of the A2 α -helix with respect to the B₅ pentamer plane for the two
120 toxins. This gross angular difference results in distinct positioning of the A subunit for CT and
121 LT, an important and previously overlooked structural feature. Lastly, protein docking analysis
122 suggests that these tertiary structural differences between LT and CT constitute a key factor
123 modulating the mode of PDI-toxin interaction, toxin disassembly and toxicity.

124

125 RESULTS

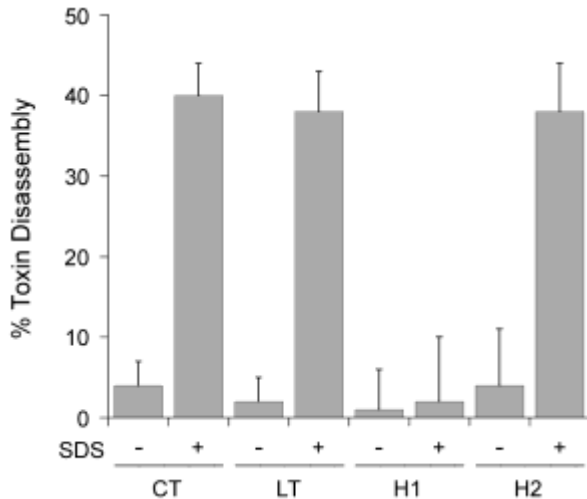
126 **CT and LT differ in toxicity and PDI-driven toxin disassembly but not overall stability.** We
127 first verified the differential cellular activities of the toxin preparations. CT exhibited greater
128 potency than LT in producing cAMP in cultured CHO cells (Fig. 1). At the highest toxin
129 concentration, the LT-induced cAMP response was ~50% of that induced by CT and was
130 roughly equivalent to the response obtained with a 10-fold lower concentration of CT. Thus, both
131 toxins were active and displayed the expected distinct cellular potencies.

132



143 **Figure 1.** Comparative analysis of CT/LT potency. CHO cells were incubated with 0.01 nM, 0.1
144 nM, or 1.0 nM CT or LT for 2 h before cAMP levels were quantified. Data are expressed as
145 percentages of the maximal cAMP response for the assay and are presented as mean \pm standard
146 error of six independent experiments with triplicate samples.

147

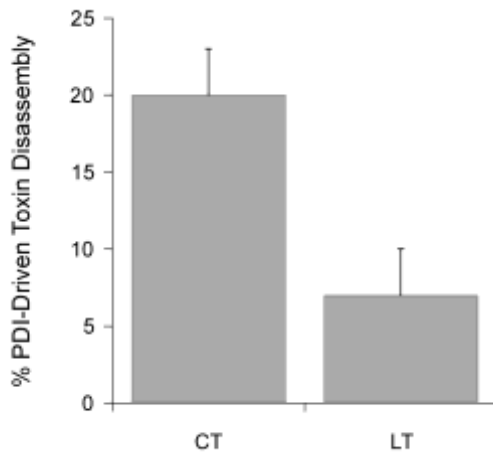


158 **Figure 2.** Comparative analysis of CT/LT stability. The indicated toxins were appended to the
 159 wells of a GM1-coated ELISA plate and exposed to pH 5.5 medium in the absence or presence
 160 of 0.1% SDS for 30 min at 25°C. After extensive washing, sequential incubations with primary
 161 and HRP-conjugated secondary antibodies were used to detect the A1 subunit. The percentage of
 162 toxin disassembly was calculated from the maximum A1 signal obtained from the corresponding
 163 untreated holotoxin. H1 represents a hybrid CTA1(CTA2)LTB₅ toxin; H2 represents a hybrid
 164 CTA1(LTA2)LTB₅ toxin. Error bars present the standard error of the means from five
 165 independent experiments with six replicate wells per condition.
 166

167 Different potencies for CT and LT were originally attributed to the more stable A2/B₅ contact
 168 for CT than for LT. However, the data supporting this model were generated with CT/LT hybrid
 169 toxins rather than the native toxins¹³. We therefore compared the relative stabilities of CT and
 170 LT using the same ELISA that was previously applied to the CT/LT hybrid toxins (Fig. 2). For
 171 this assay, we also generated our own versions of the two CT/LT hybrid toxins that were
 172 previously studied: the H1 hybrid contained the CTA subunit and the LTB pentamer, while the
 173 H2 hybrid contained the CTA1 subunit, a mutant CTA2 subunit with the LTA2 sequence
 174 between residues 226-236, and the LTB pentamer. Our hybrids contained a C-terminal KDEL
 175 sequence as opposed to the RDEL sequence in the original hybrid toxins, but this difference does
 176 not contribute to differential toxicity¹³. CT, LT, and the two hybrid toxins were each appended to
 177 a 96-well plate coated with GM1 ganglioside, which is the cell surface receptor for both toxins.
 178 The high-affinity interaction between GM1 and the B₅ pentamer prevents toxin release from the
 179 plate and places the holotoxin in a biologically meaningful orientation. An antibody recognizing
 180 the A1 subunit was then used, along with a secondary antibody conjugated to horseradish
 181 peroxidase (HRP) and 3,3',5,5'-Tetramethylbenzidine (TMB) substrate, to document the
 182 presence of the toxin-anchored A1 subunit. The ELISA was also performed with parallel samples
 183 of toxin that had first been exposed to pH 5.5 medium or 0.1% SDS in pH 5.5 medium. Acidified
 184 medium alone did not result in an appreciable loss of A1 subunit from any toxin, which was
 185 consistent with the previous study that only used the H1 and H2 toxins¹³. That study reported the
 186 addition of 0.5% SDS to pH 5.5 medium was required to detect a difference in toxin stability,
 187 with the H1 hybrid exhibiting a greater level of stability (i.e., less disassembly) than the H2

188 hybrid. We replicated that general observation here, recording essentially no disassembly of the
189 H1 hybrid and ~40% disassembly of the H2 hybrid in pH 5.5 medium containing 0.1% SDS.
190 However, we found no difference between the disassembly of CT and LT under the same
191 condition. Both wild-type toxins exhibited the same level of stability, which was comparable to
192 the stability of the H2 hybrid. These data question the validity of extrapolating the stabilities of
193 H1 (thought to represent CT) and H2 (thought to represent LT) to the stabilities of native toxins.
194 Factors other than toxin stabilities must therefore be responsible for the distinct cellular
195 potencies of CT and LT.

196



205

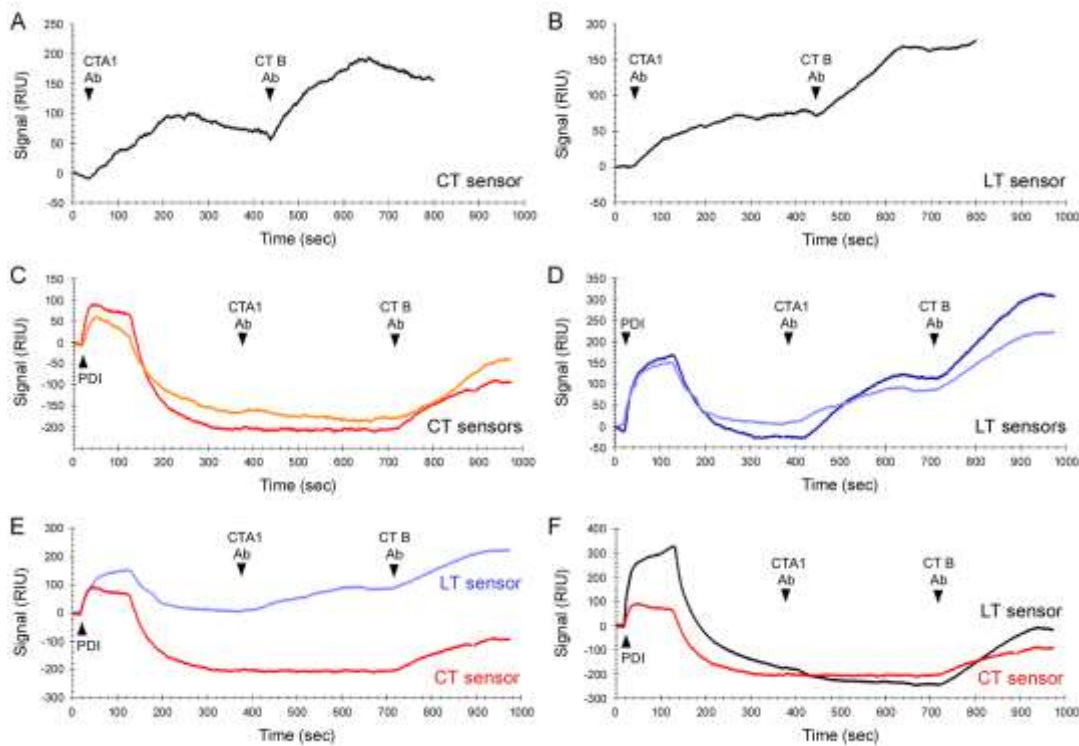
206 **Figure 3.** Comparative analysis of CT/LT disassembly by PDI. CT and LT were appended to
207 the wells of a GM1-coated ELISA plate and exposed to reduced PDI for 1 h at 37°C. After
208 extensive washing, sequential incubations with primary and HRP-conjugated secondary
209 antibodies were used to detect the A1 subunit. The percentage of toxin disassembly was
210 calculated from the maximum A1 signal obtained from the corresponding untreated holotoxin.
211 Error bars present the standard error of the means from four independent experiments with six
212 replicate wells per condition.
213

214 PDI is responsible for the disassembly of CT and is necessary for CT intoxication¹⁸. PDI
215 is also required for LT intoxication (manuscript in preparation), but the PDI-driven disassembly
216 of LT has not been documented. We accordingly examined the efficiency of CT and LT
217 disassembly by PDI with an ELISA protocol similar to the toxin stability assay (Fig. 3). The
218 toxins were again captured in a 96-well plate coated with GM1. For this assay, however, the
219 toxins were exposed to PDI rather than acidified medium with detergent. An interaction with
220 PDI releases the A1 subunit from the plate-anchored A2/B₅ complex, which is detected through
221 the loss of A1 signal²⁰. With this assay, we found that PDI disassembles CT with greater
222 efficiency than LT. A 1 h incubation with PDI released 20 ± 3% of CTA1 from its holotoxin,
223 whereas only 7 ± 3% of LTA1 was displaced from its holotoxin. This was a statistically
224 significant difference, with a *p* value of 0.015 (Student's *t* test). The higher cellular potency of
225 CT thus correlates with more efficient PDI-driven toxin disassembly for CT than for LT.

226 A second assay based on surface plasmon resonance (SPR) measurements confirmed the
227 differential disassembly of CT and LT by PDI (Fig. 4). The toxins were captured on GM1-

228 coated SPR sensors, with preliminary measurements establishing the baseline refractive index
 229 unit (RIU) corresponding to the mass of the bound holotoxin. This baseline was set as 0 RIU.
 230 Control experiments confirmed antibodies against CTA1 and CTB recognized both CT (Fig. 4A)
 231 and LT (Fig. 4B), which was expected given the high level of identity between the two toxins¹.

232



247 **Figure 4.** Relative kinetics of CT/LT disassembly by PDI. CT or LT was appended to a GM1-
 248 coated SPR sensor, and a baseline measurement corresponding to the mass of the sensor-bound
 249 holotoxin was taken to establish the 0 RIU signal. (A-B) Antibodies against the CTA1 and CTB
 250 subunits were perfused over a CT-coated (A) or LT-coated (B) sensor as indicated. (C-D) Buffer
 251 containing 1 μ M PDI and 1 mM DTT was added to a CT-coated (C) or LT-coated (D) sensor.
 252 This was followed by sequential injections of antibodies against the A1 and B subunits as
 253 indicated. Results from two independent experiments are shown for each toxin. (E) Traces for
 254 one CT disassembly experiment (red, from panel C) and one LT disassembly experiment (light
 255 blue, from panel D) are overlaid for comparative purposes. (F) An LT disassembly experiment
 256 performed with 10 μ M PDI in the perfusion buffer (black) is overlaid with a CT disassembly
 257 trace (red, from panel C).

258

259 Binding was documented through the elevated RIU signals generated after antibody perfusion
 260 over the toxin-captured sensor. If toxin disassembly occurred upon exposure to PDI, the A1
 261 subunit would be released from its holotoxin and removed from the sensor by the flow of the
 262 perfusion buffer. The RIU would consequently drop to a point below the starting value of the
 263 intact holotoxin, and no signal would be generated by subsequent injection of the CTA1
 264 antibody. We have previously reported these observations for PDI-treated CT¹⁸⁻²² and replicated

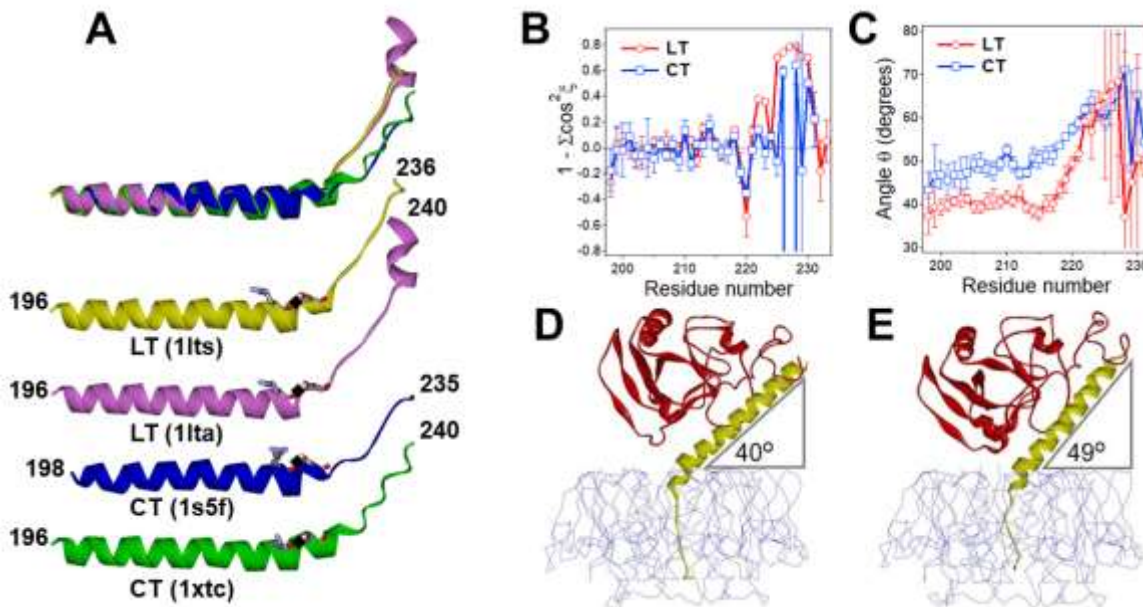
265 the result here: after an increase in RIU resulting from the binding of PDI to CT, the signal
266 dropped significantly below the initial baseline value (Fig. 4C). Exposure of the PDI-treated
267 toxin to sequential injections of CTA1 and CTB antibodies only produced a signal for the CTB
268 antibody. This demonstrated that the A1 subunit had been specifically, and completely, removed
269 from the sensor. In contrast, the RIU signal for PDI-treated LT only dropped to around the
270 initial baseline level (Fig. 4D). Elevated signals were generated from subsequent injections of
271 the A1 and B antibodies, indicating the presence of a large fraction of intact holotoxin on the LT
272 sensor 400 sec after its exposure to PDI. A direct comparison of the LT and CT data highlighted
273 the lower efficiency of LT disassembly in comparison to CT disassembly (Fig. 4E). The use of
274 10 μ M PDI improved the kinetics and extent of LT disassembly, such that it closely
275 approximated the kinetics of CT disassembly by 1 μ M PDI and resulted in a complete loss of
276 LTA1 from the sensor (Fig. 4F). These data documented the PDI-driven disassembly of LT, but
277 the complete disassembly of LT required a higher concentration of PDI than was necessary for
278 the disassembly of CT.

279 Both the ELISA and SPR disassembly assays found that holotoxin disassembly by PDI is
280 less efficient for LT than CT. Complete CT disassembly was recorded for the SPR assay,
281 whereas only partial disassembly of CT occurred with the ELISA assay. We have previously
282 noted this difference²⁰ and attribute the greater extent of toxin disassembly in the SPR assay to
283 technical differences between the two assays: the additional shear force provided by the SPR
284 perfusion buffer likely facilitates PDI-driven toxin disassembly.

285 **Analysis of structural differences between CT and LT.** The higher purported stability of CT
286 was originally explained by the helical structure of the A2 tail and its extensive direct contact
287 with the B₅ pore¹³, reported in the first X-ray crystal structure of CT (PDB ID 1xtc)¹¹. However,
288 later crystal structures of CT in various crystal forms¹⁰ reported a different, extended structure
289 for the A2 tail, resembling that of LT more than the 1xtc structure of CT (Fig. 5A), practically
290 invalidating this explanation. The geometry of the latter CT structures was also greatly improved
291 in comparison to the original structure, as noted by Heggelund et. al.¹. Here, we show by
292 comparing crystal structures from different crystal environments that the major, reliable
293 structural difference between CT and LT is not the A2 tail's secondary structure but rather the
294 larger angle between the A2 main α -helix and the B₅ pentamer plane for CT compared to LT.
295 Furthermore, we show that this tertiary structural difference translates into a different positioning
296 of the whole A domain with respect to the B₅ pentamer. This structural feature results in distinct
297 modes of PDI binding and disassembly of CT and LT, which plays a major role in differential
298 toxicities of these two otherwise structurally similar toxins.

299 The first step toward this goal was the assessment of the detailed geometry of the A2 subunit
300 using an analytic geometry algorithm specifically developed for this purpose²³. The α -helix was
301 divided into overlapping quadruplets, i.e., 4 consecutive amino acid residues from 1 to 4, 2 to 5
302 and so forth, along the whole A2 chain. The three direction cosines ($\cos \xi$) of the helical axis of
303 each quadruplet were simulated using the C α atom coordinates and the parameters for a
304 canonical α -helix, e.g., 1.5 Å rise per residue along the helical axis. The dependence of the
305 direction cosines on the amino acid residue numbers identified the degree of curvature of the
306 helix, while the criterion $1 - \Sigma \cos^2 \xi_i = 0$ determined the local α -helical quality for overlapping 4-
307 residue segments (see Supplementary Figure S1 online). Significant deviations of $1 - \Sigma \cos^2 \xi_i$
308 from zero (by more than ± 0.2) indicate non- α -helical geometry. These data are summarized in

309 Supplementary Figure S1 for six LT structures and six CT structures, and the averaged values of
 310 $1 - \sum \cos^2 \xi_i$ for LT and CT A2 chains are shown in Fig. 5B. The structures were selected to
 311 include wild-type toxins free of ligands and with ligands bound to the receptor-binding B₅
 312 pentamer, as well as toxins with point mutations in the A1 subunit, as detailed in Table 1. For all
 313 structures, $1 - \sum \cos^2 \xi_i$ displays significant deviations from zero starting at residue 220, indicating
 314 departure from α -helical geometry beyond that point (Supplementary Figure S1 and Fig. 5B).
 315 (Note that data for residue i apply to a stretch from i to $i + 3$; see above.) This is consistent with
 316 the observation that a H-bonding between Arg220 carbonyl oxygen and Ser224 side chain
 317 contributes to the tilt of the A2 chain⁵, as shown in Fig. 5A. Also notable is that in no case the
 318 direction cosines are constant in the main helical region of A2 (Supplementary Figure S1),
 319 indicating curved A2 α -helices for all structures. For LT structures, the A2 chain returns to a
 320 helical geometry for C-terminal residues 232-240 (Supplementary Figure S1).

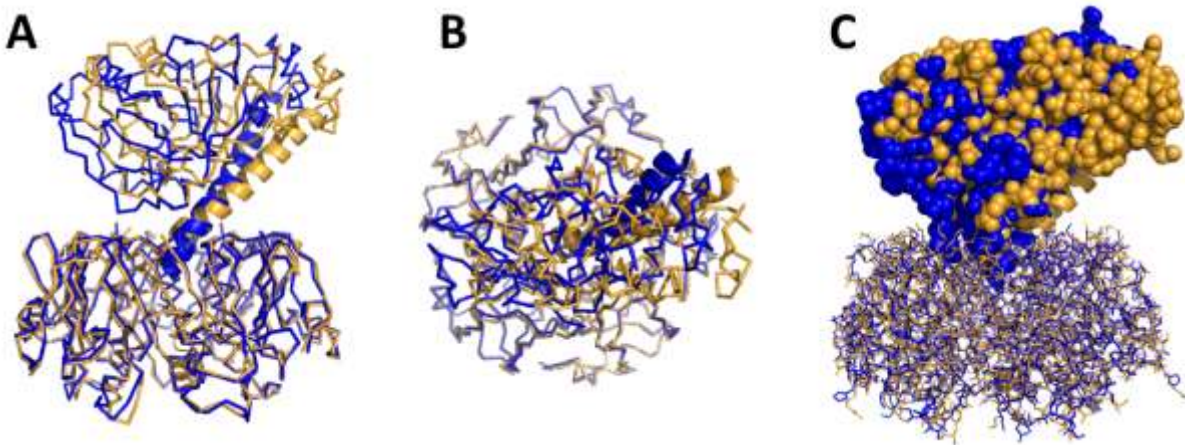


321
 322 **Figure 5.** The A2 subunit orientation dictates the positioning of the A domain on the B₅
 323 homopentamer. (A) A2 subunits of two LT structures and two CT structures are shown
 324 superimposed (top) and separately, in solid ribbon format. N- and C-terminal residue numbers, as
 325 well as respective PDB ID's are shown. H-bonds between Arg220 main chain C=O and Ser224
 326 side chain OH are presented as black rectangles. (B) Variation of $1 - (\cos^2 \xi_1 + \cos^2 \xi_2 + \cos^2 \xi_3)$
 327 along the A2 chain identifies deviations from canonical α -helical structure of the A2 subunits.
 328 (C) Changes of the angle θ between the A2 helical axis and the B₅ homopentamer plane along
 329 the A2 chain of CT and LT, as indicated. In panels B and C, average data for six CT and six LT
 330 structures (see Table 1), with standard deviations, are shown. The maximum differences in θ
 331 were 2.6 degrees within the set of LT structures and 2.4 degrees within the set of CT structures.
 332 For each amino acid residue number i , the respective ordinate value applies to a quadruplet from
 333 i to $i + 3$. (D, E) The 1lts structures of LT (D) and the 1s5f structure of CT (E) are shown to
 334 highlight the average tilt angles of the A2 domain relative to the B₅ domain. The A1, A2, and B₅

335 parts of the toxins are shown as red solid ribbon, yellow solid ribbon, and C_{α} trace, respectively.
336 Images in **A**, **D**, **E** have been rendered by Viewer Lite 4.2.

337
338 Next, the angle θ between the main helix of A2 and the B_5 plane was simulated using the C_{α}
339 atom coordinates (see Methods for details). Again, the angles were determined for overlapping
340 quadruplets and plotted as a function of residue numbers (Fig. 5C). Tilt angles, averaged for six
341 LT and six CT structures, show striking difference between A2 helix orientations in LT and CT
342 structures, i.e. a significantly larger θ angle for CT than LT (Fig. 5C). Since the helical structure
343 continues up to residue 221 (Fig. 5A), the angles of all amino acid quadruplets for each
344 individual structure were averaged from residue 200 to 221, as summarized in Table 1. The
345 average of these average values was $\theta = 49.1^{\circ} \pm 0.87^{\circ}$ for CT and $\theta = 40.5^{\circ} \pm 0.93^{\circ}$ for LT ($p <$
346 0.0001). Averaging for all 114 quadruplets of CT and those for LT yielded larger standard
347 deviations: $\theta = 49.1^{\circ} \pm 3.1^{\circ}$ for CT and $\theta = 40.5^{\circ} \pm 2.0^{\circ}$ for LT but p value in the same range ($p <$
348 0.0001), again documenting statistically significant difference between the A2 orientation for LT
349 and CT, irrespective of crystal forms, ligands bound to the B_5 pentamer, or mutations in the A1
350 chain. Also, the A2 helical tilt angle gradually increases between residues 200 and 213 for CT
351 whereas it is relatively constant for LT (note that data at residue 210 apply to the quadruplet 210-
352 213). This tertiary structural difference is illustrated in ribbon structures of LT and CT
353 holotoxins in Fig. 5D,E.

354 This 9-degree difference sustains along the A2 main helix, up to residue number 218. After
355 that, the A2 helix undergoes significant bending in preparation to enter the B_5 pore, more severe
356 for LT than CT (Fig. 5C). The angle θ gradually increases to $\sim 60^{\circ}$ at residue numbers 224-225,
357 then the simulations crash, producing meaningless values with very large deviations due to the
358 loss of the helical structure, as indicated by strong divergence of $1 - \sum \cos^2 \xi_i$ from zero (Fig. 5B).



359 **Figure 6.** Superimposed structures of CT (blue) and LT (gold) (PDB ID's 1s5f and 1lts,
360 respectively. B_5 pentamers of the two structures have been superimposed using the Align
361 function of PyMOL to underscore the different A2 subunit orientations (**A**: side view, **B**: top-
362 down view) and distinct geometric positioning of the A1 subunits (**C**). Protein main chains in (**A**)
363 and (**B**) are shown in "simple" format except that A2 domains are in ribbon format. In (**C**), the
364 B_5 pentamer is shown in "lines" format and the A1 and A2 chains in "spheres" and ribbon
365 formats, respectively. Images are generated by PyMOL 1.8.6.0 (Schrödinger, LLC).

366
367
368
369
370
371
372
373
374
375
376
377
378
379
380

As seen from these data, the important structural difference between CT and LT is not the secondary structure of the A2 tail but the overall tertiary structure of these toxins, namely, the orientation of the A2 subunit. Significantly different bending of the A2 chains of CT and LT results in distinct interdomain architectures of these toxins, i.e., specific positioning of the entire A subunit with respect to the B₅ pentamer. These differences are highlighted in Fig. 6, which shows the CT and LT structures with superimposed B₅ pentamers. The distinct angles of CTA2 (blue) and LTA2 (gold) in relation to the B₅ pentamer are evident from the side view of the toxins (Fig. 6A), but differences can also be seen from a top-down view which reveals a more curved helix for the A2 subunit of CT than LT (Fig. 6B). The differing A2 architectures, in turn, shift the relative positions of the A1 subunits such that LTA1 has a greater forward tilt than CTA1 (Fig. 6C). These crucial structural features are proposed to determine special, distinct modes of PDI binding to the toxin, as shown in the next section.

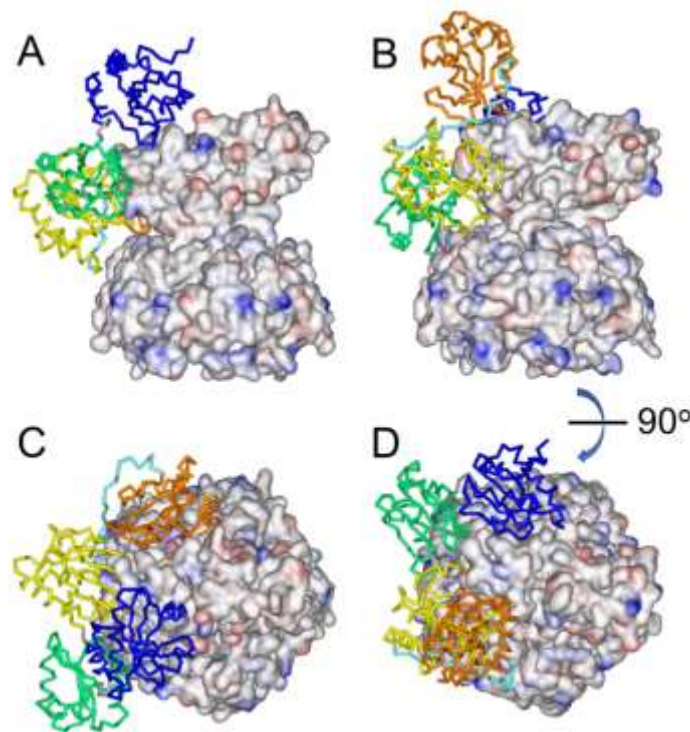
381 **Analysis of PDI-toxin interaction by protein docking simulations.** The next step was to
382 analyze the structural basis for more efficient disassembly of CT by PDI compared to LT, as
383 shown in Fig. 7. PDI-toxin docking data were obtained using the ClusPro server. The reduced
384 structure of PDI (PDB entry 4ekz)²⁴ was used for this analysis because only reduced PDI
385 interacts with CT^{17, 18}. For each pair (i.e., PDI-CT and PDI-LT), ClusPro provided 30 PDI-toxin
386 structures. We have shown earlier that the functional PDI-toxin interaction involves the A1
387 domain of CT, and that the first 133 residues of this domain constitute the major PDI binding
388 motif¹⁸. Based on this criterion, most structures have been dismissed as they were biologically
389 irrelevant. Two structures for PDI-LT and one structure for PDI-CT displayed extensive
390 interaction between PDI and the toxin's A1 chain. In these structures, PDI was wrapped around
391 the A1 subunit, trying to squeeze into the A1/B₅ corner (Fig. 7A,B). There were two major
392 structural differences between the PDI-CT and PDI-LT complexes: i) PDI orientation when
393 bound to CT was antiparallel compared to its structure when bound to LT (Fig. 7C,D), and ii)
394 PDI fit into the A1/B₅ corner of LT better than that of CT. The latter feature is expected as the
395 tertiary structure of LT provides a ~9° wider A1/B₅ corner for PDI binding compared to CT, but
396 the antiparallel binding of PDI to the two toxins is an unexpected result. The important finding,
397 however, is the significantly different mode of PDI-toxin interaction for CT and LT, which
398 obviously has important functional implication, as discussed below.

400 DISCUSSION

401 CT is more potent than LT^{12, 13}. This difference has been attributed to the non-catalytic A2
402 subunit¹³, but the underlying molecular mechanism remains unknown. The original hypothesis
403 that the A2 tail of CT provides a stronger interaction with the B₅ pentamer and thereby imparts a
404 higher stability and toxicity to CT^{13, 14} is no longer valid because i) later, improved CT structures
405 show an A2 tail structure similar to that of LT (Fig. 5A,D,E) and ii) direct examination of native
406 CT and native LT did not detect any difference in toxin stability (Fig. 2). Other factors, including
407 interactions with host chaperones, must be taken into consideration.

408 Our approach focused on the overall 3-dimensional structures of CT and LT and their
409 molecular interactions with PDI, a key chaperone required for their cellular activation¹⁸. Cell-
410 based assays, ELISA measurements, and an SPR system identified correlations between CT and
411 LT toxicities and PDI-mediated disassembly of the toxins (Figs. 1, 3, 4). Molecular simulations

412 demonstrated that distinct positioning of the CT and LT A domains determines PDI binding in
413 unique configurations. PDI fits into the wider A1/B₅ cleft of LT with relative ease, except for the
414 **a'** domain, whereas in the case of CT the whole **a** domain hangs outside of the cleft (Fig. 7). It
415 should be emphasized that the structures generated by ClusPro are based on rigid-body fitting,
416 whereas these proteins, especially PDI^{25, 26}, are flexible macromolecules rather than rigid bodies.
417 Thus, the structures of the PDI-CT and PDI-LT complexes shown in Fig. 7 should be considered
418 as starting points and combined with the earlier finding that PDI partially unfolds and expands
419 upon binding to the A1 subunit of CT¹⁹. Expansion of PDI in a tighter A1/B₅ cleft of CT will
420 exert a stronger dislodging force than in case of LT, resulting in a more efficient disassembly of
421 CT.



422
423
424
425
426
427
428
429
430
431
432
433
434
435

436 **Figure 7.** Models for interaction of reduced PDI, shown in C_α stick format, with CT (**A, C**) and
437 LT (**B, D**), shown in electrostatic surface format. (**A-B**) The toxins are presented in side-view
438 orientation. (**C-D**) The structures are rotated about a horizontal axis by 90° to generate top views.
439 Toxin surface coloring reflects the electrostatic charge: blue = positive charge, red = negative
440 charge, white = neutral. PDI coloring is domain-specific: **a** = blue; **b** = green, **b'** = yellow, **x** =
441 cyan, **a'** = orange. The structures of CT, LT, and PDI are derived from PDB entries 1s5f, 1lts,
442 and 4ekz, respectively. Images have been rendered by Viewer Lite 4.2.
443

444 The significant sequence difference at the C-terminal region of the CT and LT A2 subunits is
445 important for PDI-assisted toxin disassembly, but not because of local secondary structural
446 dissimilarities. Instead, the sequence difference in the boundary of A2 helix and A2 tail
447 determines different tilts of the A2 chain, which positions the whole A domains of the toxins at
448 specific orientations. It is interesting to note that the tilt of LTA2 has been ascribed to H-bonding
449 between Arg220 main chain carbonyl group and Ser224 side chain⁵ (1lts). This interaction

450 apparently also contributes to disruption of the A2 helical structure. However, the Arg220-
451 Ser224 H-bonding is present in all twelve LT and CT structures examined in this work (see Fig.
452 5A for some examples). The average C=O...H-O distance is 2.63 ± 0.14 Å for six CT structures
453 and 2.53 ± 0.18 Å for six LT structures, implying the difference in A2 orientation cannot be
454 explained by this H-bonding. The kink in the A2 chain following residue 220 echoes with an
455 interesting observation that LT structures in different crystal forms exhibit distinct hinge-like
456 rotations of the A2 chain, and hence the whole A subunit, around the residue Gln221, deemed to
457 be caused by crystal contacts^{4, 27}. The rotation is between 2 and 7 degrees but does not occur
458 about a certain axis, and therefore is related to the tilt angle θ discussed in this work only
459 partially. In fact, maximum differences in θ within LT structures is 2.6 degrees and that within
460 CT structures is 2.4 degrees (Table 1). These findings indicate that the statistically significant
461 difference in positioning of the A subunit with respect to the B₅ pentamer for LT and CT,
462 reported in this work, could not result from different crystal contacts, as both groups include
463 structures of different crystal forms.

464 In conclusion, distinct orientations of the A2 helix relative to the B₅ pentamer produce
465 different structures for the PDI-toxin complex for LT and CT. As demonstrated by two
466 disassembly assays and suggested by the simulations and protein docking results, the structure of
467 the PDI-CT complex results in more efficient toxin disassembly than seen for the PDI-LT
468 complex. In effect, the unique interdomain arrangements of CT and LT determine their
469 differential toxicity through specific interactions with PDI.

470

471 MATERIALS AND METHODS

472 **Materials.** Ganglioside GM1 and PDI were purchased from Sigma-Aldrich (St. Louis, MO).
473 Trypsin, soybean trypsin inhibitor, and TMB were purchased from Fisher Thermo Scientific
474 (Waltham, MA). A rabbit antibody against CTA1 was purchased from Advanced Targeting
475 Systems (Carlsbad, CA), a goat antibody against CTB was purchased from Cayman Chemicals
476 (Ann Arbor, MI), and a HRP-labeled goat anti-rabbit IgG antibody was purchased from Jackson
477 ImmunoResearch (West Grove, PA).

478

479 **Plasmids, site-directed mutagenesis and cloning.** Vector pARCT5, a gift from Dr. Randall K.
480 Holmes (University of Colorado School of Medicine, Aurora, CO), contains an arabinose-
481 inducible CT operon with signal sequences derived from the LT-IIb B gene²⁸.

482 For recombinant expression of human LT (hLT), we designed vector pARhLT5 based on
483 pARCT5, but with DNA coding for hLTA and hLTB (*Escherichia coli* strain PE0415, elt
484 operon, GenBank: EU113247.1²⁹ replacing CTA and CTB (signal sequences from the LT-IIb B
485 gene remain unchanged). The DNA was synthesized by Genscript (hLT-pUC57) and cloned into
486 pARCT5, in which an NcoI restriction site (in the *chloramphenicol* gene) was removed by a
487 silent mutation (Q5® Site-Directed Mutagenesis Kit, New England Biolabs, Ipswich, MA) using
488 primers Mut 1 and 2 (Table 2) and an annealing temperature of 64°C. Mutated pARCT5 was
489 linearized with NcoI (FastDigest, Fisher Thermo Scientific). The gel-purified vector (QIAquick
490 Gel Extraction Kit, Qiagen, Hilden, Germany) was treated with rSAP (New England Biolabs),
491 before inserting the hLT DNA fragment using T4 DNA Ligase (Thermo Scientific). pARhLT5
492 was sequenced (GATC Biotech, Konstanz, Germany) using primers Seq1–3 (Table 2).

493 To clone the H1 hybrid toxin (CTA/LTB chimera), plasmids pARCT5 and pARCT5hLT
494 were digested with NheI and HindIII (Thermo FastDigest). The pARCT5-derived vector (8184
495 bp) and the pARCT5hLT-derived insert (1316 bp) were gel purified and ligated using T4 DNA
496 Ligase. The resulting plasmid pARCTALTB was sequenced using primers Seq1, 4 and 5 (Table
497 2). An analytical restriction digest with NcoI resulted in the expected bands on a gel.

498 To generate the H2 hybrid toxin (CTA(EVDIY)/LTB chimera), site-directed mutagenesis
499 (Q5® Site-Directed Mutagenesis Kit, New England Biolabs) was performed using
500 pARCTALTB, primers Mut 3 and 4 (Table 2), and an annealing temperature of 59°C. Successful
501 mutagenesis was verified by Sanger sequencing using primers 1, 4 and 5 (Table 2).

502

503 **Expression and purification of holotoxins.** Protein expression and purification of holotoxins
504 was performed as described previously³⁰. Briefly, the genes for human LT, CT, H1 hybrid toxin,
505 and H2 hybrid toxin were expressed in OverExpress™ C43 (DE3) cells (Sigma-Aldrich). Cells
506 were grown at 37°C in TB medium containing chloramphenicol until an OD_{600 nm} of 2.0 was
507 reached. Cells were then induced with L-arabinose and harvested after 3 h. Holotoxins were
508 extracted from the bacterial pellet by inducing periplasmic lysis with polymyxin B sulfate
509 (Sigma-Aldrich). Holotoxins were purified by TALON affinity chromatography using a HiTrap
510 TALON crude column (GE Healthcare, Chicago, IL) and size exclusion chromatography with a
511 HiLoad 16/60 Superdex 200 prep grade column (GE Healthcare) equilibrated with phosphate-
512 buffered saline. To reduce B-pentamer contamination due to partially overlapping peaks, only
513 size exclusion fractions prior to the holotoxin peak maximum were pooled, filtered and stored at
514 4°C. The hybrid toxins were characterized by SDS-PAGE analysis, tryptic digestion and mass
515 spectrometry. Before use, holotoxins at 1 µg/mL concentrations were nicked with 1 µg/mL of
516 trypsin for 30 min at 25°C. Trypsin inhibitor (2 µg/mL) was then added to the toxin.

517

518 **Toxicity assay.** As previously described¹⁸, CHO cells were incubated with nicked toxin for 2 h
519 before an ELISA-based kit (GE Healthcare) was used to quantify intracellular cAMP. Basal
520 cAMP levels from unintoxicated cells were also calculated and subtracted from the values for
521 toxin-treated cells. The data were expressed as percentages of the maximal cAMP response for
522 the experiment, which was generated by 100 ng/mL of CT, corresponding to 1.23 nM.

523

524 **ELISA assays.** GM1 (6 µg/mL in ethanol) added in 50 µL volume to the wells of a 96-well plate
525 was allowed to air dry overnight at room temperature. The plates were then washed four times
526 with 100 µL of phosphate-buffered saline (pH 7.4) containing 0.05% Tween 20 (PBS-T) before
527 adding 100 µL of toxin at 1 µg/mL in PBS-T with 2.5% bovine serum albumin (BSA) or, for the
528 background control, PBS-T with 2.5% BSA alone. After 1 h at 4°C, all wells were washed four
529 times with PBS-T to remove unbound toxin from the plate. The prepared plates were then used
530 immediately.

531 For assays of toxin stability, the toxin-coated wells were exposed to McIlvaine buffer (pH
532 5.5) ± 0.1% SDS for 30 min at 25°C. This was followed by four PBS-T washes, incubation with
533 a rabbit anti-CTA1 primary antibody (100 µL at 1:1000 dilution) for 1 h at 4°C, and incubation
534 with an HRP-conjugated goat anti-rabbit IgG antibody (100 µL at 1:1000 dilution) for 30 min at

535 4°C. TMB substrate was added for 5-10 min before addition of a stop solution and absorbance
536 measurement at 450 nm with a Synergy 2 plate reader (BioTek, Winooski, VT). The percentage
537 of toxin disassembly was then calculated as $[1.00 - (\text{treated A1 signal} / \text{untreated control A1}$
538 $\text{signal})] \times 100$.

539 For assays of PDI-driven toxin disassembly, PDI (20 $\mu\text{g/mL}$) was pre-reduced with 1 mM
540 DTT for 30 min at 25°C. The toxin-coated wells were then incubated with 100 μL of PDI (2 μg
541 with 1mM DTT still present) for 1 h at 37°C before antibody processing and calculations of
542 toxin disassembly as described above for the stability assay. To establish the untreated A1
543 control signal, toxin-coated wells were exposed to 1 mM DTT in the absence of PDI. Previous
544 studies have shown that reduction alone is not sufficient for toxin disassembly¹⁶⁻¹⁸.

545

546 **SPR-based toxin disassembly assay.** Experiments were performed using a Nicoya (Kitchener,
547 ON, Canada) OpenSPR instrument. The flow rate was 20 $\mu\text{L/min}$ for all steps other than PDI
548 injection, which was performed at 40 $\mu\text{L/min}$. Volumes of 250 μL were used for each injection,
549 and all samples were placed in 10 mM MES (pH 7.4) with 200 mM NaCl. GM1 (150 $\mu\text{g/mL}$)
550 was immobilized on a gold hydrophobic sensor with OGP surface activation. This was followed
551 by two injections of PBS with 2.5% BSA. Nicked and reduced toxin (CT or LT, 10 $\mu\text{g/mL}$) was
552 then added to the GM1-coated sensor. After another injection of PBS/BSA, pre-reduced PDI (1
553 or 10 μM in buffer containing 1 mM DTT) was added to the sensor through a 150 sec injection
554 and 250 sec chase for signal stabilization. An anti-CTA1 antibody (1:1,000 dilution) was then
555 added to the sensor, which was followed by injection of an anti-CTB antibody (1:1,000 dilution).
556 Each experiment used a fresh sensor; no sensors were regenerated after the antibody additions.

557 CT and LT were nicked and reduced through a 30 min 4°C incubation in buffer
558 containing 1 mM DTT and 10 $\mu\text{g/mL}$ of trypsin. Soybean trypsin inhibitor (20 $\mu\text{g/mL}$) was then
559 added for another 30 min before toxin injection. PDI was reduced with 1 mM DTT (final
560 concentration) for 30 min at 25°C before injection. No loss of signal occurred when CT or LT
561 was exposed to DTT-containing buffer in the absence of PDI, which was consistent with
562 previous reports on the stability of reduced CT¹⁶⁻¹⁸.

563

564 **Analysis of protein interdomain orientation.** The orientation of the A2 subunit's helical axis
565 was simulated using the HELO (HELix Orientation) algorithm²³. Briefly, the C_{α} atom
566 coordinates of A2 were used to calculate the direction cosines, i.e., the cosines of angles between
567 the helical axis for four consecutive amino acid residues and the X, Y, and Z axes of the intrinsic
568 coordinate system of the protein, $\cos\zeta_1$, $\cos\zeta_2$, $\cos\zeta_3$, respectively. These cosines were simulated
569 for overlapping quadruplets along the entire A2 subunit, i.e., for residues 1-4, 2-5, 3-6..., which
570 provided the local helical orientations along the A2 chain and allowed determination of the
571 average orientation for any helical stretch.

572 Novel analytic geometry simulations were used to quantitatively describe the orientation
573 of the A2 subunit relative to the CT or LT protein molecules. This goal was achieved by
574 determining the angle between the A2 helical axis and the plane of the B₅ pentameric ring, i.e., a
575 plane made by the C_{α} atoms of identical amino acids in five units of the B₅ pentamer. We chose
576 Leu72 as such amino acid because it is located in the middle of a stable α -helix in each of B₅

577 units of both CT and LT. In 3-dimensional space, a plane can be defined by three points, whereas
 578 we actually had five points, i.e., the C α atoms of five Leu72 residues. These five points were
 579 arranged in ten (maximum possible number) triplets, and the orientations of ten planes were
 580 simulated as follows. For each triplet, the nine coordinates (x , y , and z coordinates of three C α
 581 atoms) were used to define a plane:
 582

$$583 \begin{cases} x_1 + By_1 + Cz_1 + D = 0 \\ x_2 + By_2 + Cz_2 + D = 0 \\ x_3 + By_3 + Cz_3 + D = 0 \end{cases} \quad (1)$$

584
 585 These equations were solved together to find the coefficients B, C, and D:
 586

$$587 B = \frac{(x_3 - x_1)(z_2 - z_3) + (x_2 - x_3)(z_1 - z_3)}{(y_1 - y_3)(z_2 - z_3) + (y_3 - y_2)(z_1 - z_3)} \quad (2)$$

$$588 C = \frac{x_3 - x_2 + B(y_3 - y_2)}{z_2 - z_3} \quad (3)$$

$$589 D = -x_3 - By_3 - Cz_3 \quad (4)$$

590
 591 The angles α , β , and γ between the plane normal and the X, Y and Z axes of the protein
 592 coordinate system were determined as:
 593

$$594 \alpha = \cos^{-1} \left(\frac{1}{\sqrt{1+B^2+C^2}} \right) \quad (5)$$

$$595 \beta = \cos^{-1} \left(\frac{B}{\sqrt{1+B^2+C^2}} \right) \quad (6)$$

$$596 \gamma = \cos^{-1} \left(\frac{C}{\sqrt{1+B^2+C^2}} \right) \quad (7)$$

597
 598 The angles were averaged from ten simulations to determine the mean orientation of the B₅
 599 pentamer normal. The angle between the A2 helical axis and the B₅ pentamer normal, δ , was
 600 then calculated as follows:
 601

$$602 \cos \delta = \frac{Aa + Bb + Cc}{\sqrt{(A^2 + B^2 + C^2)(a^2 + b^2 + c^2)}} \quad (8)$$

603
 604 where $A \equiv 1/\cos\beta\cos\gamma$, $B \equiv 1/\cos\alpha\cos\gamma$, $C \equiv 1/\cos\alpha\cos\beta$, $a \equiv 1/\cos\xi_2\cos\xi_3$, $b \equiv 1/\cos\xi_1\cos\xi_3$, $c \equiv$
 605 $1/\cos\xi_1\cos\xi_2$. Determination of angle δ for each quadruplet of the A2 domain revealed the
 606 variation of the helix orientation along the chain, i.e. the helical axis curvature. Moreover,
 607 application of the rule of direction cosines indicated deviations of local structures from canonical
 608 α -helical geometry. The angle θ between the A2 helix and the B₅ pentamer plane was simply $\theta =$
 609 $90^\circ - \delta$.
 610

611 **Protein-protein docking.** Protein docking simulations were conducted using an internet-based
 612 server ClusPro³¹⁻³³. Briefly, the procedure involves rigid body docking using fast Fourier
 613 transform correlation, root mean square deviation-based identification of 1000 top-ranking
 614 complexes based on energy minimization, correction of steric conflicts and refinement of best,
 615 most reliable complexes.
 616

617 **ACKNOWLEDGEMENTS**

618 We thank Dr. Randall K. Holmes (University of Colorado School of Medicine, Aurora, CO) for
619 the kind gift of pARCT5. This work was supported by the National Institutes of Health under
620 Award Numbers R03AI112854 and R01AI137056 to KT. The content is solely the
621 responsibility of the authors and does not necessarily represent the official views of the National
622 Institutes of Health.

623

624 **AUTHOR CONTRIBUTIONS**

625 A.S. and M.T. designed and performed the experiments. J.L.G. and P.C. performed the
626 experiments. J.B.H. designed and performed protein purification experiments. U.K. supervised
627 the research. K.T. supervised the research, designed the experiments, and contributed to the
628 original draft of the manuscript. S.A.T. supervised the research, designed the experiments,
629 performed analytic geometry computations, and contributed to the original draft of the
630 manuscript. All authors analyzed the data and reviewed and edited the manuscript.

631

632 **ADDITIONAL INFORMATION**

633 The authors declare no competing financial interests. Correspondence and requests for materials
634 should be addressed to S.A.T. (statulia@ucf.edu) or K.T. (Kenneth.Teter@ucf.edu).

635

636 **REFERENCES**

- 637 1. Heggelund, J. E., Bjørnstad, V. A. & Kregel, U. in *The Comprehensive Sourcebook of*
638 *Bacterial Protein Toxins*, 4th edition (eds. Alouf, J. E., Ladant, D. & Popoff, M. R.) 195-
639 229 (Elsevier, Waltham, MA, 2015).
- 640 2. De Haan, L. & Hirst, T. R. Cholera toxin: a paradigm for multi-functional engagement of
641 cellular mechanisms (Review). *Mol Membr Biol* **21**, 77-92 (2004).
- 642 3. Clemens, J. D., Nair, G. B., Ahmed, T., Qadri, F. & Holmgren, J. Cholera. *Lancet* **390**,
643 1539-1549 (2017).
- 644 4. Sixma, T. K. et al. Lactose binding to heat-labile enterotoxin revealed by X-ray
645 crystallography. *Nature* **355**, 561-564 (1992).
- 646 5. Sixma, T. K. et al. Refined structure of *Escherichia coli* heat-labile enterotoxin, a close
647 relative of cholera toxin. *J Mol Biol* **230**, 890-918 (1993).
- 648 6. Merritt, E. A., Sixma, T. K., Kalk, K. H., van Zanten, B. A. & Hol, W. G. J. Galactose-
649 binding site in *Escherichia coli* heat-labile enterotoxin (LT) and cholera toxin (CT). *Mol*
650 *Microbiol* **13**, 745-53 (1994).
- 651 7. van den Akker, F. et al. The Arg7Lys mutant of heat-labile enterotoxin exhibits great
652 flexibility of active site loop 47-56 of the A subunit. *Biochemistry* **34**, 10996-11004
653 (1995).
- 654 8. Van Den Akker, F., Steensma, E. & Hol, W. G. J. Tumor marker disaccharide D-Gal-
655 β 1,3-GalNAc complexed to heat-labile enterotoxin from *Escherichia coli*. *Protein Sci* **5**,
656 1184-1188 (1996).

- 657 9. van den Akker, F., Pizza, M., Rappuoli, R. & Hol, W. G. J. Crystal structure of a non-
658 toxic mutant of heat-labile enterotoxin, which is a potent mucosal adjuvant. *Protein Sci* **6**,
659 2650–2654 (1997).
- 660 10. O'Neal, C. J., Amaya, E. I., Jobling, M. G., Holmes, R. K. & Hol, W. G. J. Crystal
661 structures of an intrinsically active cholera toxin mutant yield insight into the toxin
662 activation mechanism. *Biochemistry* **43**, 3772-82 (2004).
- 663 11. Zhang, R. G. et al. The three-dimensional crystal structure of cholera toxin. *J Mol Biol*
664 **251**, 563-73 (1995).
- 665 12. Lencer, W. I. et al. Targeting of cholera toxin and *Escherichia coli* heat labile toxin in
666 polarized epithelia: role of COOH-terminal KDEL. *J Cell Biol* **131**, 951-62 (1995).
- 667 13. Rodighiero, C. et al. Structural basis for the differential toxicity of cholera toxin and
668 *Escherichia coli* heat-labile enterotoxin. Construction of hybrid toxins identifies the A2-
669 domain as the determinant of differential toxicity. *J Biol Chem* **274**, 3962-9 (1999).
- 670 14. Craft, J. W., Jr., Shen, T. W., Brier, L. M. & Briggs, J. M. Biophysical characteristics of
671 cholera toxin and *Escherichia coli* heat-labile enterotoxin structure and chemistry lead to
672 differential toxicity. *J Phys Chem B* **119**, 1048-1061 (2015).
- 673 15. Majoul, I., Ferrari, D. & Soling, H. D. Reduction of protein disulfide bonds in an
674 oxidizing environment. The disulfide bridge of cholera toxin A-subunit is reduced in the
675 endoplasmic reticulum. *FEBS Lett* **401**, 104-8 (1997).
- 676 16. Mekalanos, J. J., Collier, R. J. & Romig, W. R. Enzymic activity of cholera toxin. II.
677 Relationships to proteolytic processing, disulfide bond reduction, and subunit
678 composition. *J Biol Chem* **254**, 5855-61 (1979).
- 679 17. Tsai, B., Rodighiero, C., Lencer, W. I. & Rapoport, T. A. Protein disulfide isomerase acts
680 as a redox-dependent chaperone to unfold cholera toxin. *Cell* **104**, 937-48 (2001).
- 681 18. Taylor, M., Banerjee, T., Ray, S., Tatulian, S. A. & Teter, K. Protein disulfide isomerase
682 displaces the cholera toxin A1 subunit from the holotoxin without unfolding the A1
683 subunit. *J Biol Chem* **286**, 22090-100 (2011).
- 684 19. Taylor, M. et al. Substrate-induced unfolding of protein disulfide isomerase displaces the
685 cholera toxin A1 subunit from its holotoxin. *PLoS Pathogens* **10**, e1003925 (2014).
- 686 20. Cherubin, P. et al. Protein disulfide isomerase does not act as an unfoldase in the
687 disassembly of cholera toxin. *Biosci Rep* **38**, pii: BSR20181320 (2018).
- 688 21. Reddy, S. et al. Grape extracts inhibit multiple events in the cell biology of cholera
689 intoxication. *PLoS One* **8**, e73390 (2013).
- 690 22. Guyette, J. et al. Quercetin-3-rutinoside blocks the disassembly of cholera toxin by
691 protein disulfide isomerase. *Toxins* **11**, pii: E458. (2019).
- 692 23. Tatulian, S. A. Determination of helix orientations in proteins. *Comput Biol Chem* **32**,
693 370-374 (2008).
- 694 24. Wang, C. et al. Structural insights into the redox-regulated dynamic conformations of
695 human protein disulfide isomerase. *Antioxid Redox Signal* **19**, 36-45 (2013).
- 696 25. Freedman, R. B. et al. 'Something in the way she moves': The functional significance of
697 flexibility in the multiple roles of protein disulfide isomerase (PDI). *Biochim Biophys*
698 *Acta Proteins Proteom* **1865**, 1383-1394 (2017).
- 699 26. Guyette, J., Evangelista, B., Tatulian, S. A. & Teter, K. Stability and conformational
700 resilience of protein disulfide isomerase. *Biochemistry* **58**, 3572-3584 (2019).
- 701 27. Sixma, T. K. et al. Heat-labile enterotoxin crystal forms with variable A/B5 orientation
702 Analysis of conformational flexibility. *FEBS Lett* **305**, 81-85 (1992).

703 28. Jobling, M. G., Palmer, L. M., Erbe, J. L. & Holmes, R. K. Construction and
704 characterization of versatile cloning vectors for efficient delivery of native foreign
705 proteins to the periplasm of Escherichia coli. *Plasmid* **38**, 158-73 (1997).

706 29. Lasaro, M. A. et al. Genetic diversity of heat-labile toxin expressed by enterotoxigenic
707 *Escherichia coli* strains isolated from humans. *J Bacteriol* **190**, 2400-2410 (2008).

708 30. Heim, J. B., Hodnik, V., Heggelund, J. E., Anderluh, G. & Krengel, U. Crystal structures
709 of cholera toxin in complex with fucosylated receptors point to importance of secondary
710 binding site. *Sci Rep* **2**, 12243. doi: 10.1038/s41598-019-48579-2. (2019).

711 31. Kozakov, D. et al. How good is automated protein docking? *Proteins* **81**, 2159-2166
712 (2103).

713 32. Kozakov, D. et al. The ClusPro web server for protein-protein docking. *Nature Protocols*
714 **12**, 255-278 (2017).

715 33. Vajda, S. et al. New additions to the ClusPro server motivated by CAPRI. *Proteins* **85**,
716 435-444 (2017).

717 34. van den Akker, F. et al. Crystal structure of a new heat-labile enterotoxin, LT-IIb.
718 *Structure* **4**, 665-678 (1996).

719
720
721
722
723

754 **Table 2.** DNA oligonucleotide sequences.

DNA oligo name DNA sequence (changed bases in bold)

Mut1	CCGTTTTCACTATGGGCAAATATTATAC
Mut2	GGGCGAAGAAGTTGTCCA
Mut3	TATATATA AATAGAATTAAGGATGAATTATGATTTAAG
Mut4	TCCACTTC AGATTGATAGCCTGAAAATATTTG
Seq1	CAA GAG ATT ACG CGC AGA CC
Seq2	CTT GGA GAG AAG AAC CCT GG
Seq3	TGC CGC GAC TCT CTA TAA TTT C
Seq4	GAT CTT GGA GCA TTC CCA CA
Seq5	TTA TAG CCA CTG CAC CCA ACA TG

755

Supplementary Files

This is a list of supplementary files associated with this preprint. Click to download.

- [SI.pdf](#)